Eur. Phys. J. A **18**, 117–127 (2003)
DOI 10.1140/epja/i2003-10061-y

THE EUROPEAN PHYSICAL JOURNAL A

Low-energy photoproduction of ω-mesons

J. Barth[1,a], W. Braun[1,b], J. Ernst[2], K.-H. Glander[1], J. Hannappel[1], N. Jöpen[1], H. Kalinowsky[2,b], F.J. Klein[1,3], F. Klein[1,c], E. Klempt[2], R. Lawall[1], J. Link[2,b], D. Menze[1], W. Neuerburg[1,b], M. Ostrick[1], E. Paul[1], H. van Pee[2], I. Schulday[1], W.J. Schwille[1,d], B. Wiegers[1,b], F.W. Wieland[1], J. Wißkirchen[1,b], and C. Wu[1]

[1] Physikalisches Institut, Bonn University, Bonn, Germany
[2] Helmholtz-Institut für Strahlen- und Kernphysik, Bonn University, Bonn, Germany
[3] CUA, Department of Physics, Washington D. C., USA

Received: 26 February 2003 / Revised version: 20 May 2003 /
Published online: 9 October 2003 –
Communicated by M. Garçon

Abstract. The photoproduction of the vector meson ω has been studied between threshold and $W = 2.4$ GeV with the SAPHIR detector at the Bonn electron stretcher ring ELSA. Besides, the total cross-sections angular distributions in the CMS and decay angular distributions in the helicity and Gottfried-Jackson systems have been measured.

PACS. 14.40.Cs Properties of specific particles: Other mesons with $S = C = 0$, mass < 2.5 GeV

1 Introduction

Photoproduction of vector mesons at photon energies beyond 3 GeV generally is regarded to be governed by diffraction or "pomeron exchange". However, for the ω production Ballam *et al.* [2] already evaluated from their bubble chamber data that the unnatural-parity exchange contribution stemming from a π^0 in the t-channel for photon energies between 3 and 5 GeV is of the same order of magnitude as the natural-parity exchange contribution from the pomeron exchange. Thus, close to threshold a strong π^0 contribution was to be expected. Of particular interest in this energy region is the quest for contributions from s-channel resonances and the search for the so-called "missing resonances" [3]. The ωp system is an ideal choice to identify resonance contributions due to the narrow width (8 MeV) of the $\omega(783)$ and the restriction to $I = \frac{1}{2}$ resonances.

In this experiment we measured the total and differential cross-sections from threshold up to $E_\gamma = 2.6$ GeV. The decay angular distributions in the Gottfried-Jackson and helicity systems were determined in four energy ranges, dividing the transfered squared four-momentum $|t|$ into two domains.

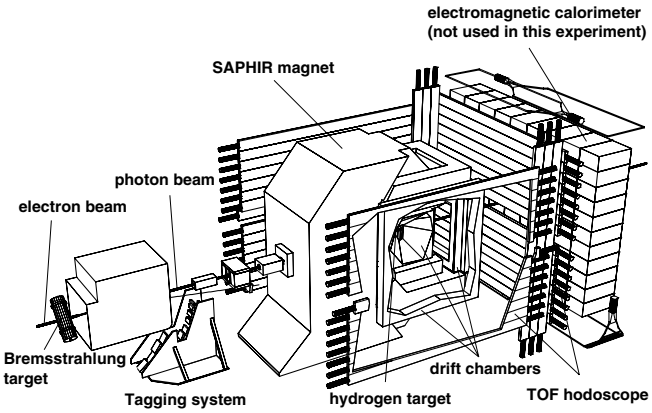

Fig. 1. Sketch of the SAPHIR detector.

2 Experimental method

The SAPHIR detector [4], shown schematically in fig. 1, is a multi-purpose magnetic spectrometer with a large angular acceptance consisting of a tagging facility, drift chambers and a scintillator wall for triggering and time-of-flight measurements. The detector covers the full polar angular range from 0° to 180°, the accepted solid angle is limited to approximately $0.6 \times 4\pi$ sr due to the magnet pole pieces. The ELSA electron beam produces photons via bremsstrahlung in a copper foil target. The energies of the corresponding scattered electrons are determined in the tagging system for photon energies from 31% to 94% of the incident electron energy (up to 2.8 GeV).

[a] Part of doctoral thesis [1].
[b] No longer working at this experiment.
[c] e-mail: klein@physik.uni-bonn.de
[d] e-mail: schwille@physik.uni-bonn.de

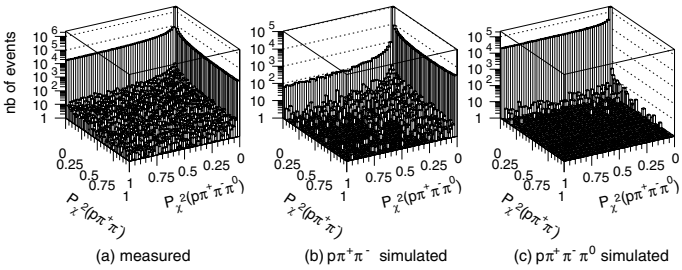

Fig. 2. Crosstalk histograms on the separation of $p\pi^+\pi^-\pi^0$ and $p\pi^+\pi^-$ final states.

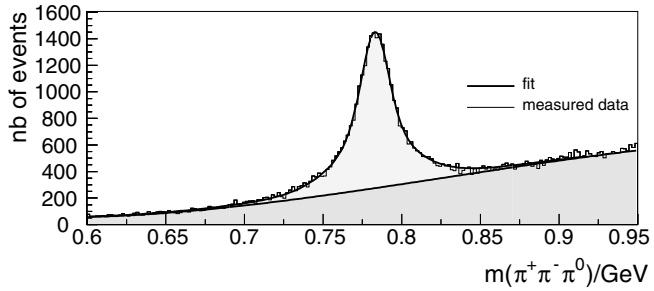

Fig. 3. ω separation from the background in the $\pi^+\pi^-\pi^0$ mass spectrum.

In coincidence with a photon counter behind the electromagnetic calorimeter (not visible in the figure), the tagging system also measures the effective photon flux (see sect. 3) passing through the production target consisting of a cylindrical polyimide film (125 μm thick) container, 3 cm in diameter and 8 cm in length filled with liquid hydrogen. It is surrounded by 14 cylindrical layers (partially stereo layers) of the central drift chamber, where all outgoing charged particles are detected. Their tracks are bent in the field of a C-shaped magnet which allows a measurement of momentum and charge. The momentum resolution $\Delta p/p$ for 300 MeV/c particles in the central drift chamber is approximately 2.5%. In the forward direction a planar drift chamber ameliorates the momentum resolution to about 1%. The surrounding scintillator wall determines the time of flight (ToF) of a particle and provides, together with the measured momentum, information on its mass. The momentum detection threshold for charged pions starts at 50 MeV/c, for protons at 150 MeV/c, mainly depending on the position of the production vertex in the target. The momentum-dependent detection efficiencies were measured and found to be consistent with those from simulated data.

3 Photon flux normalisation

The photon flux is measured using the tagging system and the photon veto counter. The tagging system comprises 14 scintillation counters for triggering and time definition and 2 multi-wire proportional chambers defining 703 energy channels. Each scintillation counter is connected to a scaler. Approximately every 0.4 seconds a minimum bias trigger defined by an electron that hits a counter in the tagging system starts a full read-out of the SAPHIR data including the scalers. This event sample is used to calculate a normalisation factor, based on N_e as the number of hits in all tagging scintillators and N_{γ_i} as the number of coincidences between the photon veto counter, the energy channel i, and the associated tagging scintillator. Multiplying the ratio N_{γ_i}/N_e by the total number of hits in the tagging scintillators for a run period provides the photon flux for the channel i. Thus, since data taking and flux normalisation take place simultaneously, any inefficiency of the tagger, even if it varies during the data acquisition, is automatically taken into account.

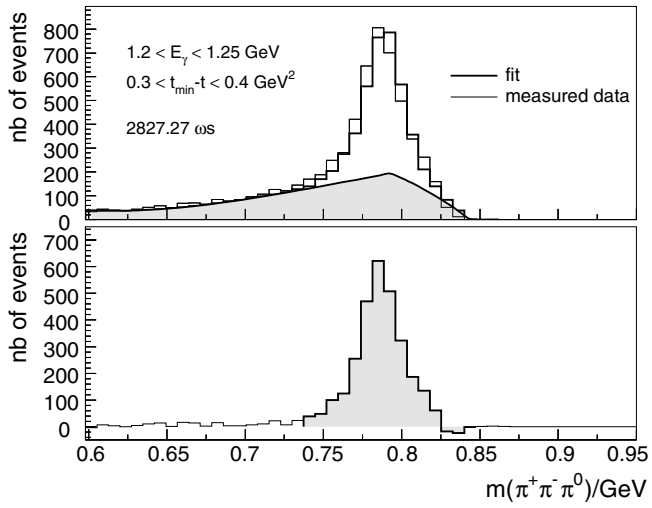

Fig. 4. ω separation from the background in the $\pi^+\pi^-\pi^0$ mass spectrum in a critical kinematic region and resulting ω signal.

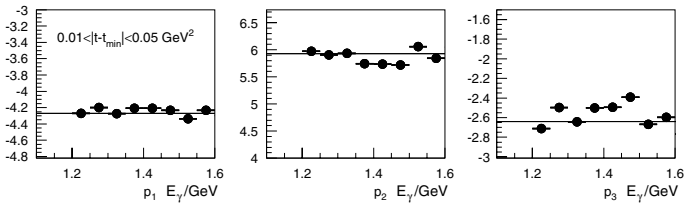

Fig. 5. Coefficients of the background polynomial $u(m) = a(1 + p_1 m + p_2 m^2 + p_3 m^3)$ as a function of the photon energy in the t range $0.01 < |t - t_{\min}| < 0.05$ GeV^2.

4 Data reduction and determination of the cross-sections

The raw data (133 million events) stem from 3 data taking periods in 1997 and 1998 with an ELSA electron energy of 2.6 and 2.8 GeV, respectively. Hence, photon energies vary from below reaction threshold up to 2.65 GeV. The trigger required two hits in the ToF wall together with a signal in the photon tagging system. All triggered events are passed through a reconstruction software which delivers energy and momenta of the outgoing particles. The ω-meson is identified by its decay into one neutral and two charged pions; therefore we select $p\pi^+\pi^-\pi^0$ final states in

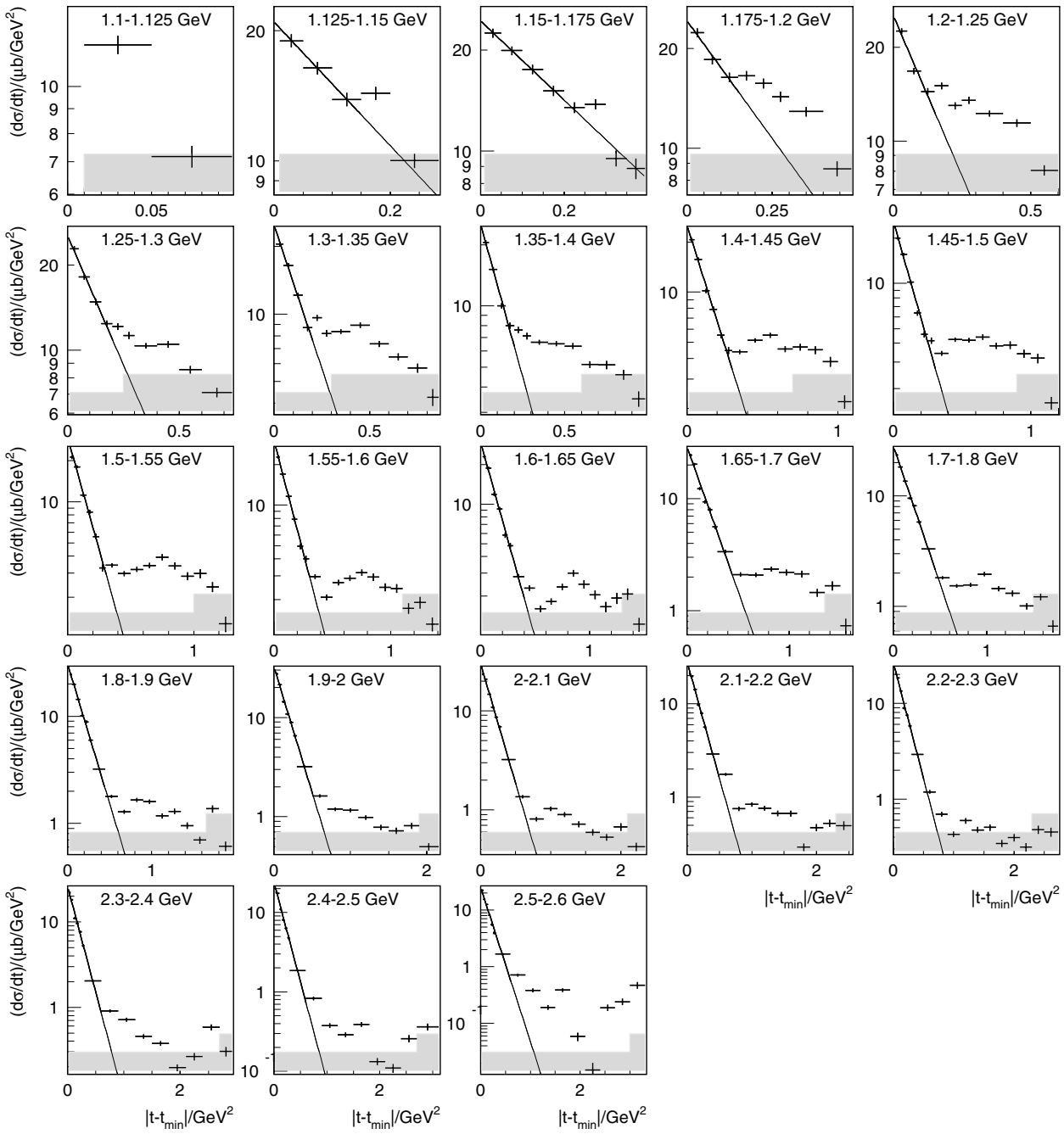

Fig. 6. Differential cross-sections $\mathrm{d}\sigma/\mathrm{d}t$ for incident photon energies from reaction threshold up to 2.6 GeV. The shaded areas indicate the systematic errors (see text).

our data. Starting from three-prong events, we test various reaction hypotheses by kinematical fits, mainly: $\gamma p \to p\pi^+\pi^-$, $\gamma p \to pK^+K^-$, $\gamma p \to p\pi^+\pi^-\pi^0$, $\gamma p \to n\pi^+\pi^+\pi^-$, $\gamma p \to pK^+\pi^-$, $\gamma p \to pK^+\pi^-\pi^0$ and $\gamma p \to pe^+e^-$. For the analysis, those with the maximum value for the χ^2 probability for the $p\pi^+\pi^-\pi^0$ final state were selected.

The crosstalk histograms (fig. 2) for the separation of $p\pi^+\pi^-$ and $p\pi^+\pi^-\pi^0$ final states exemplarily show the uncritical assignment to these two processes. For measured data (fig. 2(a)) a rather flat χ^2 probability distribution for the $p\pi^+\pi^-\pi^0$ hypothesis is clearly visible at $P_{\chi^2} = 0$ for the $p\pi^+\pi^-$ hypothesis and vice versa, allowing a good separation between the two processes. Simulated $p\pi^+\pi^-$ events are suppressed by a factor 50 in the $p\pi^+\pi^-\pi^0$ channel (fig. 2(b)). Since these events show no enhancement of the $\pi^+\pi^-\pi^0$ invariant mass in the ω region, the effective suppression for the ω separation is even better. More importantly, virtually no $p\pi^+\pi^-\pi^0$ events are lost into the $p\pi^+\pi^-$ channel (fig. 2(c)). In order to check contributions from $\gamma p \to p\pi^+\pi^-(n\pi^0)$, $n > 1$, we examined the $(p\pi^+\pi^-)$ missing-mass distribution from the selected $p\pi^+\pi^-\pi^0$ events and found no masses above the π^0 mass.

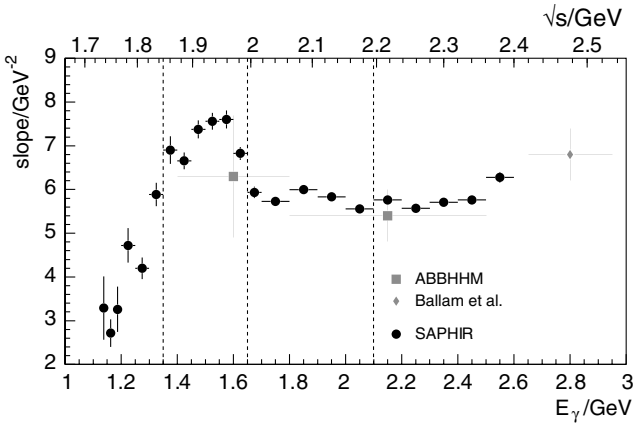

Fig. 7. Slope parameters b as a function of the photon energy E_γ, compared to results of earlier experiments [2,5]. The three vertical dashed lines indicate the four photon energy regions used for the decay angular distributions shown in figs. 12 and 13 below.

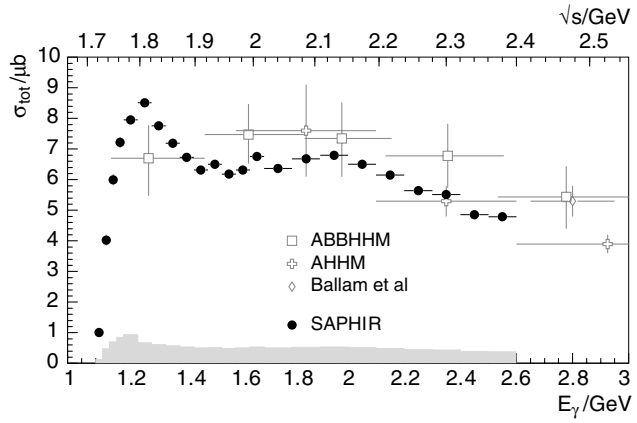

Fig. 8. Total cross-section of the reaction $\gamma p \to p\omega$ compared to results of earlier experiments [2,5,6]. The shaded area indicates the systematic errors in μbarn.

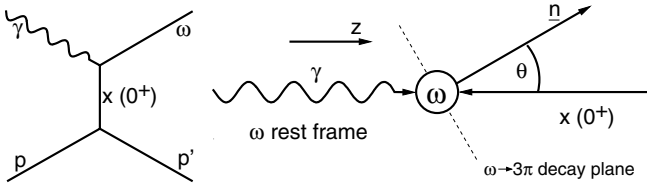

Fig. 9. The Gottfried-Jackson frame.

Figure 3 shows the ω signal in the $\pi^+\pi^-\pi^0$ mass spectrum above a continuous background consisting of other reactions leading to final states with one neutral and two charged pions.

The ω signal can be separated from the background by fitting a polynomial of 3rd order together with an appropriate signal function. Figure 3 shows that a convolution of a Breit-Wigner shape with the natural decay width [7] and two Gaussians, reflecting the experimental resolution (double Voigt function) yields a perfect description. This separation method was applied for each kine-

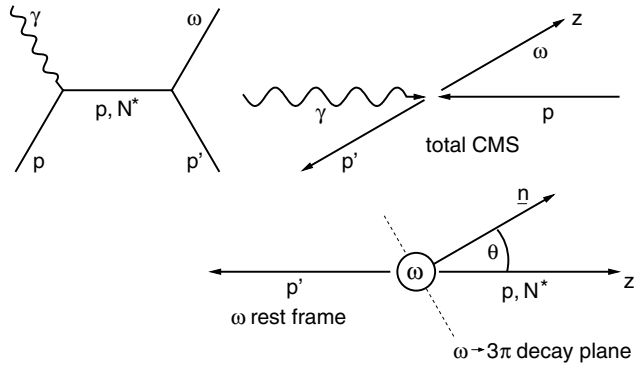

Fig. 10. The helicity frame.

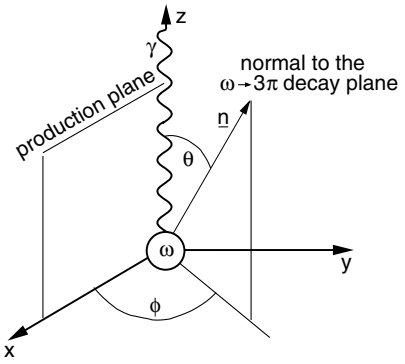

Fig. 11. Azimuthal and polar angles in the Gottfried-Jackson frame.

matical bin (E_γ, t) and (E_γ, $\cos\theta$), t being the squared four-momentum transfer and θ the decay angle in the ω CMS. It has the advantage to be independent of any special assumption concerning the background. However, in some (E_γ, t)-bins this method is not applicable because events with invariant 3-pion masses beyond the ω mass are kinematically excluded, leaving the fit unconstrained (fig. 4). In these cases we used a different method; it is based on the observation that the polynomial coefficients p_1, p_2 and p_3 for the background mass distribution $u(m) = a(1 + p_1 m + p_2 m^2 + p_3 m^3)$ taken from kinematically well-constrained fits exhibit only a weak dependence on E_γ and t, allowing a safe extrapolation towards the critical (E_γ, t)-bins. By using these extrapolated coefficients the background at lower $\pi^+\pi^-\pi^0$ masses can be described well. In fig. 5 the extrapolation towards lower photon energies is shown exemplarily for $0.01 < |t - t_{\min}| < 0.05$ GeV^2. The fall-off (fig. 4) towards large masses in the data reflects the kinematical limit of $p\pi^+\pi^-\pi^0$ production and can be described via simulated and reconstructed phase space production, its position depends on the kinematical region. Together with $\omega \to 3\pi$ mass distributions from simulated, tracked and reconstructed events the separation could be done satisfactorily (fig. 4). We estimate the systematic errors of this method to be 10%, whereas the error of the above-described simple background separation for uncritical t regions is below 5%. These errors are indicated by the shaded areas in fig. 6, the larger ones indicating the kinematically more difficult regions.

Table 1. Spin density matrix elements in the Gottfried-Jackson frame.

E_γ	$\lvert t-t_{\min}\rvert$	ϱ_{00}	ϱ_{1-1}	ϱ_{10}
1.1–1.35 GeV	< 0.2 GeV^2	0.3017 ± 0.0348	-0.0067 ± 0.0306	-0.0738 ± 0.0192
	> 0.2 GeV^2	0.6167 ± 0.0399	-0.0063 ± 0.0252	-0.0692 ± 0.0222
1.35–1.65 GeV	< 0.3 GeV^2	0.1290 ± 0.0315	0.0305 ± 0.0348	0.0302 ± 0.0180
	> 0.3 GeV^2	0.5525 ± 0.0390	-0.0139 ± 0.0282	-0.0966 ± 0.0225
1.65–2.1 GeV	< 0.3 GeV^2	0.2233 ± 0.0330	0.0324 ± 0.0318	0.0721 ± 0.0180
	> 0.3 GeV^2	0.4405 ± 0.0429	-0.0102 ± 0.0339	-0.0339 ± 0.0252
2.1–2.6 GeV	< 0.3 GeV^2	0.2370 ± 0.0345	0.0531 ± 0.0345	0.0772 ± 0.0192
	> 0.3 GeV^2	0.4608 ± 0.0435	0.0284 ± 0.0354	-0.0726 ± 0.0267

Table 2. Spin density matrix elements in the helicity system.

E_γ	$\lvert t-t_{\min}\rvert$	ϱ_{00}	ϱ_{1-1}	ϱ_{10}
1.1–1.35 GeV	< 0.2 GeV^2	0.3133 ± 0.0051	-0.0001 ± 0.0042	-0.0036 ± 0.0030
	> 0.2 GeV^2	0.2868 ± 0.0069	-0.1350 ± 0.0057	-0.0846 ± 0.0042
1.35–1.65 GeV	< 0.3 GeV^2	0.2702 ± 0.0063	0.0977 ± 0.0051	-0.0582 ± 0.0033
	> 0.3 GeV^2	0.2616 ± 0.0066	-0.1316 ± 0.0054	-0.0728 ± 0.0039
1.65–2.1 GeV	< 0.3 GeV^2	0.2020 ± 0.0051	0.0220 ± 0.0045	-0.0705 ± 0.0027
	> 0.3 GeV^2	0.2867 ± 0.0072	-0.0681 ± 0.0060	-0.0639 ± 0.0042
2.1–2.6 GeV	< 0.3 GeV^2	0.1604 ± 0.0060	0.0202 ± 0.0057	-0.0534 ± 0.0033
	> 0.3 GeV^2	0.2509 ± 0.0096	-0.0528 ± 0.0084	-0.0486 ± 0.0054

The acceptance of the detector was determined via Monte-Carlo–generated events and determined in every (E_γ, t)-bin for the differential cross-section and every $(E_\gamma, \cos\theta)$-bin for the decay angular distributions, respectively. After generating an event of the desired type, the created particles were tracked through the SAPHIR detector by an adapted version of CERN's GEANT, considering particle decays, energy losses, multiple scattering and the experimentally determined efficiencies of the detector components, *e.g.* the drift chambers and the scintillator hodoscopes. The generation starting with a preset $\exp(-bt)$ distribution led to new b values from the data, which were used as new input for the next iteration. After applying this procedure twice, no further variation in the determined b values was observed. For very small generated $|t-t_{\min}|$ the proton has a momentum too low to be detected and the acceptance approaches zero. Therefore we evaluated the differential cross-sections starting from $|t-t_{\min}| \geq 0.01$ GeV^2. The values in the uncovered $|t-t_{\min}|$ range were fixed by exponential extrapolation. The total cross-sections were then calculated by integration over the exponential fall-off part of $\mathrm{d}\sigma/\mathrm{d}t$ and adding the contents of the bins at larger $|t-t_{\min}|$ values.

Besides the systematic error due to the background separation as discussed above we estimate the errors coming from flux normalisation and target thickness to be less than 2% and 3%, respectively. The uncertainty resulting from acceptance calculations amounts to 5%.

5 Results and interpretation

The differential cross-sections $\mathrm{d}\sigma/\mathrm{d}t$ were evaluated in 23 energy bins. They are shown in fig. 6 together with an exponential fit of the form $\mathrm{d}\sigma/\mathrm{d}t = a \cdot \exp(-b|t-t_{\min}|)$ to the data points at low $|t|$ values. This fit was performed up to the value of $|t-t_{\min}|$, where deviations from the exponential are clearly noticeable. The fit regions are indicated by bold lines. The energy dependence of the resulting slope parameters b is presented in fig. 7 and table 6.

In the differential cross-sections (fig. 6, tables 3-5) one observes, besides the exponential fall-off at small $|t|$ values, rather strong contributions that cannot be explained by t-channel "pomeron" or π^0 exchanges. The total cross-section (fig. 8, table 6) shows a pronounced maximum of 8.5 μb around a photon energy of 1.3 GeV.

For vector mesons decay angular distributions examine production mechanism hypotheses. Various reference systems are in common use. In the Gottfried-Jackson system (fig. 9) the quantization axis (z) is defined as the direction of the photon in the ω rest system. The direction of the normal $\underline{n}$ to the $\pi^+\pi^-\pi^0$ plane defines the polar angle θ, and the azimuthal angle φ with respect to the production plane, see fig. 11.

The Gottfried-Jackson system is used to test the "t-channel helicity" conservation which implies that the spin of the ω is aligned along the direction of the photon. The conservation of the "s-channel helicity" is examined in the helicity system (fig. 10); here the quantization axis (z) points into the direction of the ω in the total CMS or

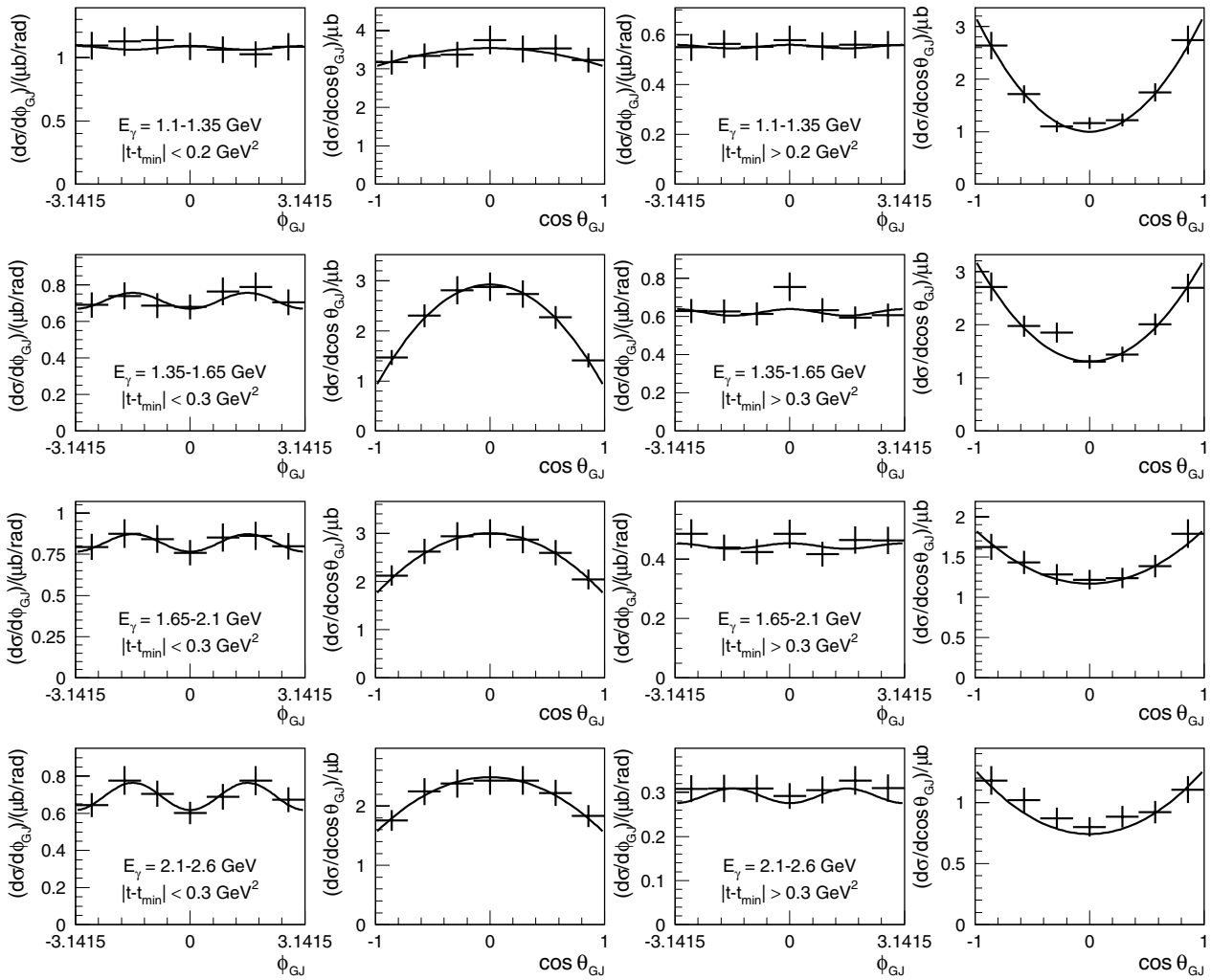

Fig. 12. Decay angular distributions in the Gottfried-Jackson frame, the two left columns show the ϕ and the $\cos\theta$ shapes for small $|t|$, the two right columns for larger $|t|$ values. The error bars indicate statistical errors.

opposite to the direction of the outgoing proton in the ω rest frame, respectively.

The full decay angular distribution for ω production with unpolarized photons can be expressed in terms of the spin density matrix elements (see, *e.g.*, [8]):

$$W(\theta,\varphi) = \frac{3}{4\pi}\Big(\frac{1}{2}(1-\varrho^0_{00}) + \frac{1}{2}(3\varrho^0_{00}-1)\cos^2\theta - \varrho^0_{1-1}\sin^2\theta\cos 2\varphi - \sqrt{2}\mathrm{Re}\varrho^0_{10}\sin 2\theta\cos\varphi\Big).$$

In both systems a $\sin^2\theta$ distribution and a flat shape in φ is observed if the spin of the ω is aligned along the z-axis. In the Gottfried-Jackson system this implies a 0^+ (pomeron) exchange. In the helicity system a $\sin^2\theta$ distribution, as observed at high energies, is generally regarded as an indication for diffractive production (see, *e.g.*, [9]). But already Gilman *et al.* [10] emphasized that, using a t-channel (*e.g.* Regge) model, one needs t-channel spin flip and non-flip contributions related in a very intricate way in order to obtain s-channel helicity conservation. Since the t-channel exchange shows a weak energy dependence, a relatively strong variation with energy observed in decay angular distributions can be taken as an indication for resonance production.

We present the $\cos\theta$ and ϕ decay angular distributions for both systems in four energy and two t ranges in figs. 12 and 13, and the corresponding spin density matrix elements in figs. 14, 15 and tables 1, 2. Compared to data from high-energy experiments [2,11], in our case obviously different production mechanisms dominate. Whilst at high energies s-channel helicity is conserved, we observe strong deviations from a $\sin^2\theta_\mathrm{H}$ for small and large $|t|$ values up to $E_\gamma = 1.65$ GeV. Above 1.65 GeV the same is true for $|t - t_\mathrm{min}| > 0.3$ GeV^2, while for small $|t|$ values the θ_H distribution tends towards a $\sin^2\theta_\mathrm{H}$ form. The SLAC measurement at 2.8 GeV [2] (fig. 16) is consistent with our results.

The slope parameter b (fig. 7) exhibits a strong energy dependence from a value of 3 GeV^{-2} at threshold to 7.5 GeV^{-2} at 1.55 GeV, then dropping to 6 GeV^{-2} at 1.65 GeV and staying nearly constant above this energy.

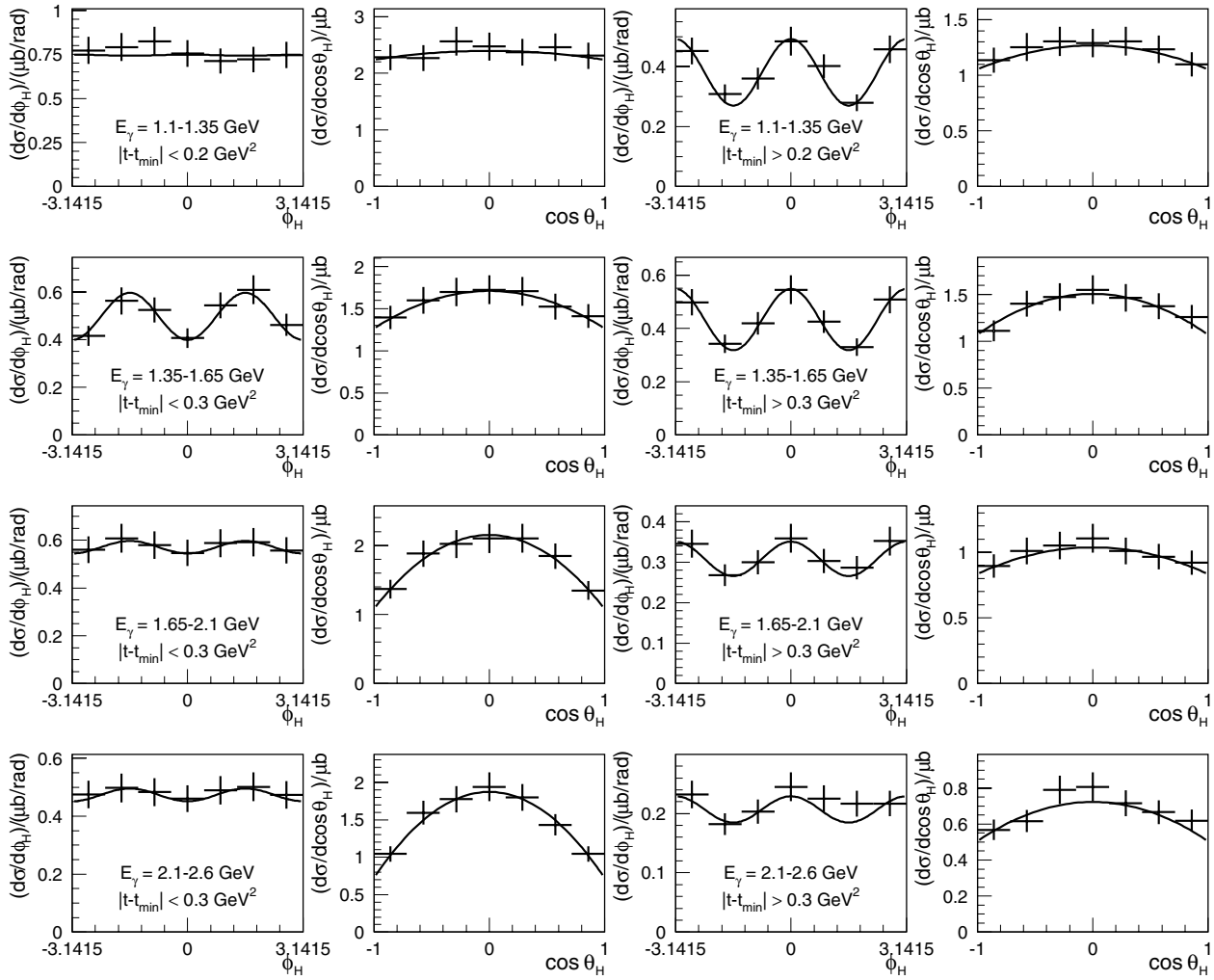

Fig. 13. Decay angular distributions in the helicity frame, the two left columns show the ϕ and the $\cos\theta$ shapes for small $|t|$, the two right columns for larger $|t|$ values. The error bars indicate statistical errors.

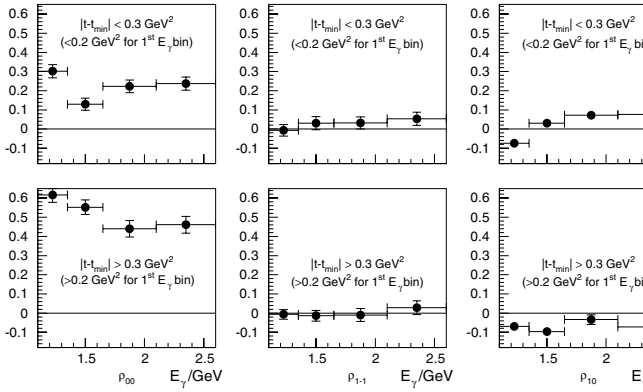

Fig. 14. Spin density matrix elements in the Gottfried-Jackson frame. The error bars indicate statistical errors.

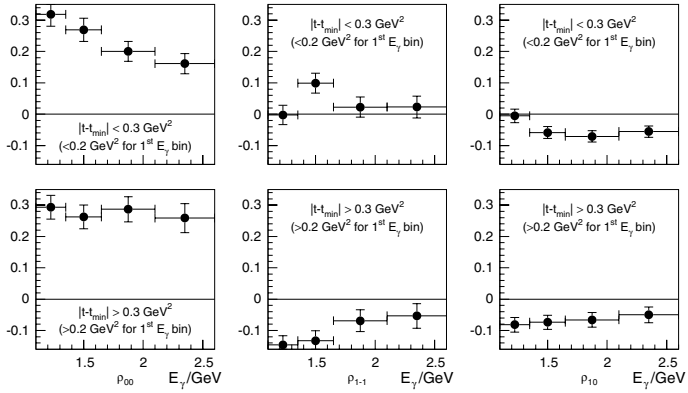

Fig. 15. Spin density matrix elements in the helicity frame. The error bars indicate statistical errors.

Neither diffractive t-channel production nor π^0 exchange can cause the observed energy behaviour. Together with the strong energy dependence of the decay angular distributions in the threshold region and the steep rise of the total cross-section from threshold to a maximum at 1.3 GeV we take this as an indication for a resonance contribution. Without polarization observables a more detailed analysis of resonance contributions as well as the question of the relative strength of the diffractive and the π^0 exchange part is only possible with the help of theoretical models.

Table 3. Differential cross-sections part 1.

$\lvert t-t_{\min}\rvert$ (GeV^2)	$\mathrm{d}\sigma/\mathrm{d}t$ (μb/GeV^2)
$E_\gamma = 1.1$–1.125 GeV	
0.01–0.05	12.19 ± 0.52
0.05–0.098	7.17 ± 0.36
$E_\gamma = 1.125$–1.15 GeV	
0.01–0.05	18.95 ± 0.65
0.05–0.1	16.39 ± 0.54
0.1–0.15	13.86 ± 0.50
0.15–0.2	14.33 ± 0.51
0.2–0.283	10.01 ± 0.37
$E_\gamma = 1.15$–1.175 GeV	
0.01–0.05	22.46 ± 0.70
0.05–0.1	19.91 ± 0.59
0.1–0.15	17.49 ± 0.55
0.15–0.2	15.12 ± 0.51
0.2–0.25	13.48 ± 0.48
0.25–0.3	13.78 ± 0.49
0.3–0.35	9.505 ± 0.513
0.35–0.393	8.871 ± 0.633
$E_\gamma = 1.175$–1.2 GeV	
0.01–0.05	22.30 ± 0.70
0.05–0.1	18.50 ± 0.57
0.1–0.15	16.35 ± 0.53
0.15–0.2	16.54 ± 0.53
0.2–0.25	15.68 ± 0.52
0.25–0.3	14.31 ± 0.50
0.3–0.4	12.90 ± 0.43
0.4–0.483	8.678 ± 0.446
$E_\gamma = 1.2$–1.25 GeV	
0.01–0.05	22.50 ± 0.50
0.05–0.1	16.76 ± 0.38
0.1–0.15	14.42 ± 0.36
0.15–0.2	15.03 ± 0.36
0.2–0.25	12.98 ± 0.34
0.25–0.3	13.50 ± 0.34
0.3–0.4	12.26 ± 0.27
0.4–0.5	11.42 ± 0.30
0.5–0.599	8.062 ± 0.309
$E_\gamma = 1.25$–1.3 GeV	
0.01–0.05	22.80 ± 0.51
0.05–0.1	18.13 ± 0.40
0.1–0.15	14.82 ± 0.37
0.15–0.2	12.42 ± 0.33
0.2–0.25	12.12 ± 0.33
0.25–0.3	11.27 ± 0.323
0.3–0.4	10.38 ± 0.234
0.4–0.5	10.49 ± 0.275
0.5–0.6	8.546 ± 0.269
0.6–0.735	7.106 ± 0.272
$E_\gamma = 1.3$–1.35 GeV	
0.01–0.05	20.51 ± 0.496
0.05–0.1	16.45 ± 0.397
0.1–0.15	12.12 ± 0.341
0.15–0.2	8.686 ± 0.288
0.2–0.25	9.616 ± 0.303
0.25–0.3	8.199 ± 0.280
0.3–0.4	8.348 ± 0.201
0.4–0.5	8.917 ± 0.240
0.5–0.6	7.353 ± 0.237
0.6–0.7	6.443 ± 0.245
0.7–0.8	5.743 ± 0.270
0.8–0.859	4.260 ± 0.370
$E_\gamma = 1.35$–1.4 GeV	
0.015–0.05	20.50 ± 0.541
0.05–0.1	15.12 ± 0.389
0.1–0.15	10.01 ± 0.316
0.15–0.2	8.020 ± 0.283
0.2–0.25	7.614 ± 0.276
0.25–0.3	7.119 ± 0.267
0.3–0.4	6.637 ± 0.178
0.4–0.5	6.529 ± 0.190
0.5–0.6	6.351 ± 0.209
0.6–0.7	5.153 ± 0.204
0.7–0.8	5.131 ± 0.234
0.8–0.9	4.586 ± 0.258
0.9–0.976	3.502 ± 0.303
$E_\gamma = 1.4$–1.45 GeV	
0.015–0.05	20.68 ± 0.55
0.05–0.1	15.74 ± 0.40
0.1–0.15	10.17 ± 0.32
0.15–0.2	7.892 ± 0.28
0.2–0.25	5.506 ± 0.23
0.25–0.3	4.463 ± 0.21
0.3–0.4	4.372 ± 0.142
0.4–0.5	5.126 ± 0.165
0.5–0.6	5.501 ± 0.194
0.6–0.7	4.556 ± 0.187
0.7–0.8	4.668 ± 0.218
0.8–0.9	4.492 ± 0.252
0.9-1	3.817 ± 0.256
1-1.088	2.197 ± 0.204
$E_\gamma = 1.45$–1.5 GeV	
0.015–0.05	19.98 ± 0.55
0.05–0.1	15.61 ± 0.41
0.1–0.15	10.19 ± 0.33
0.15–0.2	6.352 ± 0.261
0.2–0.25	4.579 ± 0.222
0.25–0.3	4.162 ± 0.211
0.3–0.4	3.419 ± 0.125
0.4–0.5	4.226 ± 0.149
0.5–0.6	4.183 ± 0.156
0.6–0.7	4.398 ± 0.182
0.7–0.8	3.852 ± 0.186
0.8–0.9	3.884 ± 0.217
0.9-1	3.411 ± 0.213
1-1.1	3.176 ± 0.230
1.1–1.197	1.600 ± 0.155
$E_\gamma = 1.5$–1.55 GeV	
0.02–0.05	21.23 ± 0.62
0.05–0.1	18.02 ± 0.44
0.1–0.15	11.18 ± 0.35
0.15–0.2	8.414 ± 0.306
0.2–0.25	5.569 ± 0.249
0.25–0.3	3.282 ± 0.191
0.3–0.4	3.429 ± 0.133
0.4–0.5	2.983 ± 0.124
0.5–0.6	3.203 ± 0.137
0.6–0.7	3.424 ± 0.157
0.7–0.8	3.934 ± 0.200
0.8–0.9	3.399 ± 0.194
0.9-1	2.858 ± 0.193
1-1.1	2.982 ± 0.228
1.1–1.2	2.385 ± 0.202
1.2–1.302	1.278 ± 0.165

Table 4. Differential cross-sections part 2.

$\lvert t-t_{\min}\rvert$ (GeV^2)	$\mathrm{d}\sigma/\mathrm{d}t$ (μb/GeV^2)
$E_\gamma = 1.55$–1.6 GeV	
0.02–0.05	22.73 ± 0.66
0.05–0.1	16.97 ± 0.44
0.1–0.15	11.61 ± 0.36
0.15–0.2	7.881 ± 0.302
0.2–0.25	4.963 ± 0.240
0.25–0.3	4.015 ± 0.216
0.3–0.4	2.958 ± 0.123
0.4–0.5	2.081 ± 0.101
0.5–0.6	2.678 ± 0.124
0.6–0.7	2.878 ± 0.139
0.7–0.8	3.168 ± 0.165
0.8–0.9	2.933 ± 0.181
0.9-1	2.469 ± 0.166
1-1.1	2.422 ± 0.176
1.1–1.2	1.728 ± 0.153
1.2–1.3	1.904 ± 0.186
1.3–1.407	1.320 ± 0.156
$E_\gamma = 1.6$–1.65 GeV	
0.02–0.05	23.00 ± 0.67
0.05–0.1	18.84 ± 0.47
0.1–0.15	11.92 ± 0.37
0.15–0.2	9.197 ± 0.331
0.2–0.25	5.819 ± 0.264
0.25–0.3	4.841 ± 0.240
0.3–0.4	2.808 ± 0.124
0.4–0.5	2.295 ± 0.113
0.5–0.6	1.598 ± 0.090
0.6–0.7	1.815 ± 0.101
0.7–0.8	2.344 ± 0.132
0.8–0.9	2.990 ± 0.176
0.9-1	2.461 ± 0.177
1-1.1	2.048 ± 0.154
1.1–1.2	1.656 ± 0.148
1.2–1.3	1.927 ± 0.186
1.3–1.4	2.075 ± 0.212
1.4–1.509	1.218 ± 0.149
$E_\gamma = 1.65$–1.7 GeV	
0.02–0.05	24.51 ± 0.71
0.05–0.1	20.36 ± 0.50
0.1–0.15	12.29 ± 0.389
0.15–0.2	9.387 ± 0.340
0.2–0.25	7.973 ± 0.313
0.25–0.3	5.615 ± 0.263
0.3–0.45	3.375 ± 0.119
0.45–0.6	2.106 ± 0.092
0.6–0.75	2.088 ± 0.098
0.75–0.9	2.354 ± 0.121
0.9–1.05	2.199 ± 0.139
1.05–1.2	2.127 ± 0.148
1.2–1.35	1.448 ± 0.117
1.35–1.5	1.671 ± 0.153
1.5–1.610	0.7323 ± 0.1147
$E_\gamma = 1.7$–1.8 GeV	
0.025–0.05	23.35 ± 0.55
0.05–0.1	18.27 ± 0.34
0.1–0.15	13.54 ± 0.29
0.15–0.2	9.510 ± 0.248
0.2–0.25	8.103 ± 0.229
0.25–0.3	5.801 ± 0.193
0.3–0.45	3.314 ± 0.083
0.45–0.6	1.820 ± 0.062
0.6–0.75	1.539 ± 0.058
0.75–0.9	1.562 ± 0.063
0.9–1.05	1.958 ± 0.087
1.05–1.2	1.451 ± 0.076
1.2–1.35	1.315 ± 0.077
1.35–1.5	1.008 ± 0.065
1.5–1.65	1.221 ± 0.087
1.65–1.759	0.6675 ± 0.0870
$E_\gamma = 1.8$–1.9 GeV	
0.025–0.05	24.53 ± 0.57
0.05–0.1	19.96 ± 0.36
0.1–0.15	14.44 ± 0.31
0.15–0.2	10.17 ± 0.26
0.2–0.25	8.895 ± 0.245
0.25–0.3	5.967 ± 0.201
0.3–0.45	3.211 ± 0.083
0.45–0.6	1.792 ± 0.065
0.6–0.75	1.287 ± 0.054
0.75–0.9	1.652 ± 0.067
0.9–1.05	1.593 ± 0.075
1.05–1.2	1.177 ± 0.065
1.2–1.35	1.295 ± 0.078
1.35–1.5	0.9555 ± 0.0658
1.5–1.65	0.6976 ± 0.0524
1.65–1.8	1.368 ± 0.103
1.8–1.956	0.6134 ± 0.0628
$E_\gamma = 1.9$–2.0 GeV	
0.025–0.05	27.46 ± 0.62
0.05–0.1	21.38 ± 0.39
0.1–0.15	14.37 ± 0.31
0.15–0.2	10.79 ± 0.27
0.2–0.25	8.953 ± 0.252
0.25–0.3	6.561 ± 0.216
0.3–0.5	3.209 ± 0.074
0.5–0.7	1.622 ± 0.056
0.7–0.9	1.194 ± 0.050
0.9–1.1	1.166 ± 0.051
1.1–1.3	0.9821 ± 0.0526
1.3–1.5	0.7819 ± 0.0475
1.5–1.7	0.7221 ± 0.0514
1.7–1.9	0.8126 ± 0.0563
1.9–2.151	0.4988 ± 0.0427
$E_\gamma = 2.0$–2.1 GeV	
0.025–0.05	23.56 ± 0.58
0.05–0.1	20.85 ± 0.39
0.1–0.15	14.73 ± 0.32
0.15–0.2	10.82 ± 0.28
0.2–0.25	8.621 ± 0.252
0.25–0.3	6.902 ± 0.225
0.3–0.5	3.239 ± 0.077
0.5–0.7	1.357 ± 0.050
0.7–0.9	0.8088 ± 0.0408
0.9–1.1	1.027 ± 0.050
1.1–1.3	0.9005 ± 0.0487
1.3–1.5	0.7184 ± 0.0476
1.5–1.7	0.5947 ± 0.0423
1.7–1.9	0.5315 ± 0.0423
1.9–2.1	0.6740 ± 0.0577
2.1–2.345	0.4261 ± 0.0398

Table 5. Differential cross-sections part 3.

$\lvert t-t_{\min}\rvert$ (GeV^2)	$\mathrm{d}\sigma/\mathrm{d}t$ (μb/GeV^2)
E_γ = 2.1–2.2 GeV	
0.03–0.05	21.12 ± 0.64
0.05–0.1	19.74 ± 0.39
0.1–0.15	14.19 ± 0.33
0.15–0.2	9.739 ± 0.277
0.2–0.25	7.903 ± 0.250
0.25–0.3	5.646 ± 0.211
0.3–0.5	2.907 ± 0.075
0.5–0.7	1.756 ± 0.063
0.7–0.9	0.7498 ± 0.0398
0.9–1.1	0.8376 ± 0.0460
1.1–1.3	0.7634 ± 0.0437
1.3–1.5	0.6723 ± 0.0440
1.5–1.7	0.6707 ± 0.0496
1.7–1.9	0.2909 ± 0.0272
1.9–2.1	0.4724 ± 0.0418
2.1–2.3	0.5268 ± 0.0480
2.3–2.537	0.4959 ± 0.0526
E_γ = 2.2–2.3 GeV	
0.03–0.05	20.34 ± 0.63
0.05–0.1	18.37 ± 0.38
0.1–0.15	13.45 ± 0.32
0.15–0.2	8.898 ± 0.265
0.2–0.25	7.514 ± 0.244
0.25–0.3	5.816 ± 0.214
0.3–0.5	2.908 ± 0.079
0.5–0.7	1.188 ± 0.049
0.7–0.9	0.6966 ± 0.0403
0.9–1.1	0.4283 ± 0.0298
1.1–1.3	0.5932 ± 0.0383
1.3–1.5	0.4761 ± 0.0341
1.5–1.7	0.5058 ± 0.0383
1.7–1.9	0.3438 ± 0.0290
1.9–2.1	0.3954 ± 0.0347
2.1–2.3	0.3154 ± 0.0321
2.3–2.5	0.4802 ± 0.0483
2.5–2.728	0.4535 ± 0.0497
E_γ = 2.3–2.4 GeV	
0.03–0.05	21.85 ± 0.67
0.05–0.1	18.03 ± 0.38
0.1–0.15	11.00 ± 0.30
0.15–0.2	9.590 ± 0.282
0.2–0.25	7.608 ± 0.251
0.25–0.3	5.276 ± 0.209
0.3–0.6	2.030 ± 0.055
0.6–0.9	0.9014 ± 0.0379
0.9–1.2	0.7185 ± 0.0373
1.2–1.5	0.4548 ± 0.0271
1.5–1.8	0.3788 ± 0.0251
1.8–2.1	0.1962 ± 0.0178
2.1–2.4	0.2650 ± 0.0254
2.4–2.7	0.5818 ± 0.0477
2.7–2.919	0.3038 ± 0.0384
E_γ = 2.4–2.5 GeV	
0.03–0.05	17.93 ± 0.66
0.05–0.1	17.29 ± 0.41
0.1–0.15	10.94 ± 0.33
0.15–0.2	8.027 ± 0.283
0.2–0.25	6.314 ± 0.251
0.25–0.3	4.807 ± 0.219
0.3–0.6	1.847 ± 0.058
0.6–0.9	0.8262 ± 0.0388
0.9–1.2	0.3753 ± 0.0250
1.2–1.5	0.2884 ± 0.0205
1.5–1.8	0.3886 ± 0.0257
1.8–2.1	0.1328 ± 0.0139
2.1–2.4	0.1094 ± 0.0137
2.4–2.7	0.2582 ± 0.0273
2.7–3.109	0.3623 ± 0.0363
E_γ = 2.5–2.6 GeV	
0.03–0.05	22.21 ± 0.83
0.05–0.1	15.45 ± 0.44
0.1–0.15	12.61 ± 0.39
0.15–0.2	8.171 ± 0.321
0.2–0.25	5.518 ± 0.264
0.25–0.3	3.969 ± 0.224
0.3–0.6	1.678 ± 0.063
0.6–0.9	0.7176 ± 0.0411
0.9–1.2	0.3839 ± 0.0294
1.2–1.5	0.1929 ± 0.0175
1.5–1.8	0.3882 ± 0.0285
1.8–2.1	0.05900 ± 0.00992
2.1–2.4	0.01509 ± 0.00507
2.4–2.7	0.1902 ± 0.0246
2.7-3	0.2410 ± 0.0309
3-3.298	0.4715 ± 0.0613

Already Friman and Soyeur [12] considered the importance of the π^0 exchange. Other authors, *e.g.* Y. Oh *et al.* [13], Q. Zhao *et al.* [14,15], Q. Zhao [16] and G. Penner and U. Mosel [17] come to the same conclusion in their analyses. Additionally, these authors take into account the nucleon exchange and s-channel resonance contributions. Furthermore Y. Oh *et al.* and Q. Zhao [16] implemented the natural-parity pomeron exchange.

The only analysis that took into account our new data on σ_{tot} and $\mathrm{d}\sigma/\mathrm{d}t$ is the coupled-channel analysis of G. Penner and U. Mosel [17].

In this analysis of photon- and pion-induced reactions they developed a unitary coupled-channel Lagrangian taking into account the final states γN, πN, 2πN, ηN, KΛ, KΣ and ωN. For the ω production this group extracts a dominating $P_{11}(1710)$-resonance together with smaller $J^P = \frac{3}{2}^+$ contributions from the $P_{13}(1720)$ and $P_{13}(1900)$ and a strong t-channel π^0 exchange. Figure 17 shows our data together with their fit and the partial-wave decomposition which is dominated by the $J^P = \frac{1}{2}^+$ ($P_{11}(1710)$) and a π^0 exchange. As mentioned above, such a strong resonance contribution is consistent with our interpretation of the measured data. In fig. 18 our angular distributions are to be seen together with the curves of Penner and Mosel.

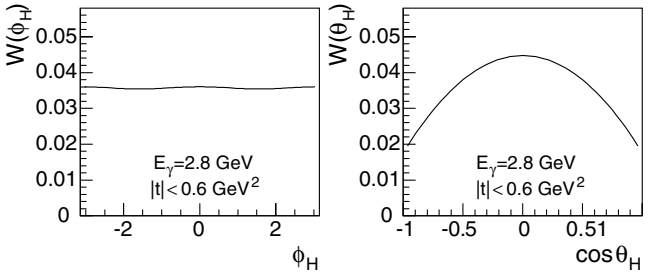

Fig. 16. Decay angular distributions in the helicity frame, evaluated from data in [2].

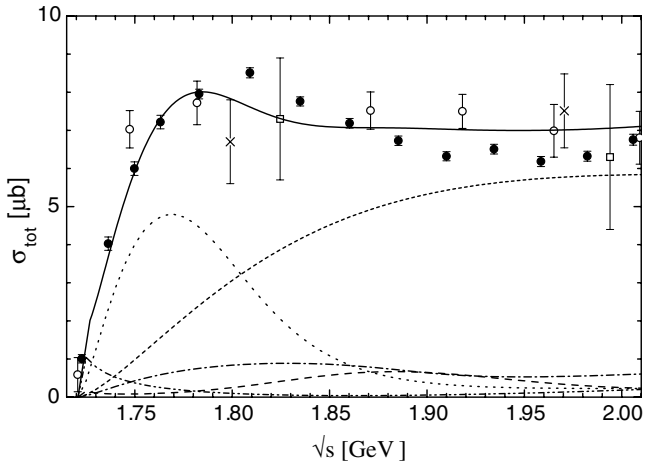

Fig. 17. $\gamma\mathrm{p} \to \omega\mathrm{p}$ total cross-section Data: ●: this experiment; ○: [18]; ×: [5]; □: [19]. Partial-wave decomposition [17]: dotted line: $J^P = \frac{1}{2}^+$; short-dashed line: $J^P \geq \frac{5}{2}^+$ (stemming from π^0 exchange); dashed line: $J^P = \frac{1}{2}^-$; dashed-dotted line: $J^P = \frac{3}{2}^+$; dashed-double-dotted line: $J^P = \frac{3}{2}^-$.

6 Summary

In summary, total and differential cross-sections and ω decay angular distributions were measured for the reaction $\gamma\mathrm{p} \to \omega\mathrm{p}$. The data show that diffraction is no longer dominant as opposed to higher energies. Obviously resonance contributions play an important role. The presented new data together with the analysis of Penner and Mosel hint at strong $P_{11}(1710)$-resonance production. Besides that π^0 exchange in the t-channel is non-negligible.

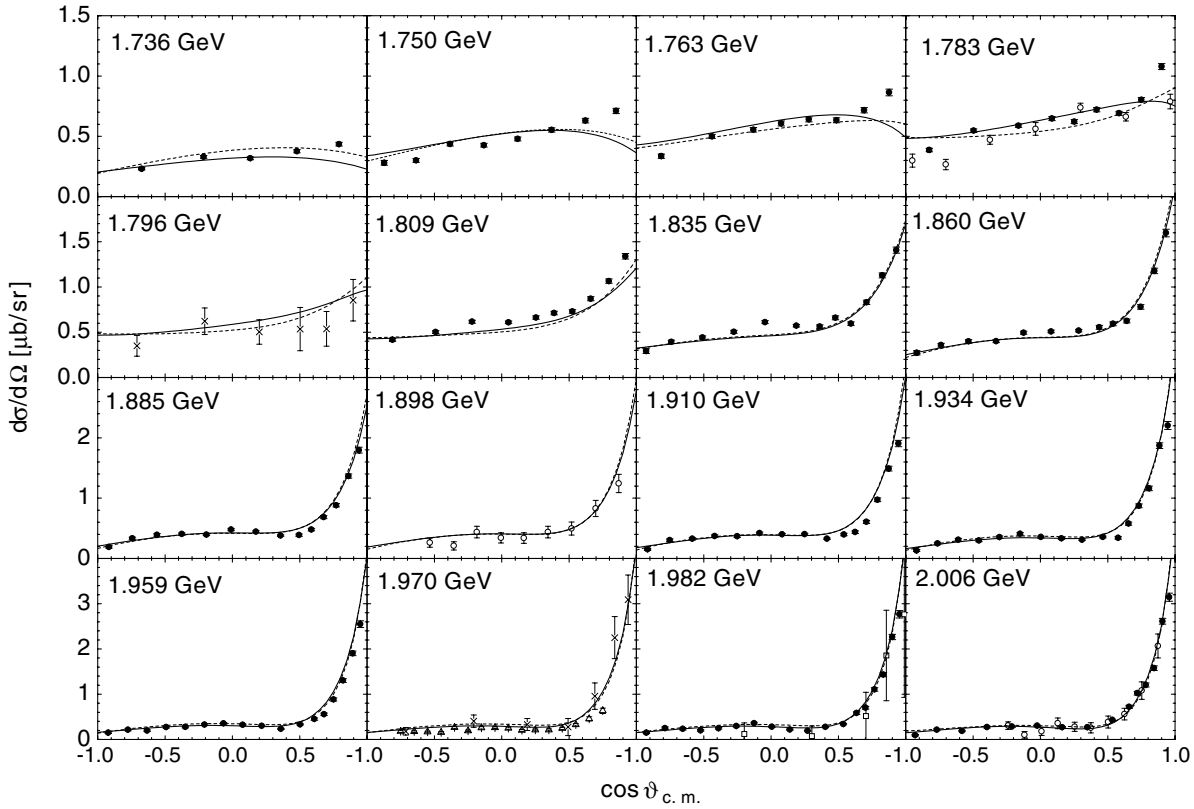

Fig. 18. $\gamma p \to \omega p$ differential cross-sections for invariant hadronic masses W from 1.736 GeV to 2.006 GeV. The lines show the fitting results for different signs of the $g_{\omega\rho\Phi}$ coupling [17]. This coupling is connected with the important t-channel exchange in $\pi N \to \omega N$. Solid line: + sign; dashed line: − sign; data: ●: this experiment; △: [20]; other data as in fig. 17.

Table 6. Total cross-sections and slopes.

E_γ (GeV)	$\sigma_{\rm tot}$ (μb)	Slope b (GeV^{-2})
1.1–1.125	1.01 ± 0.11	—
1.125–1.15	4.03 ± 0.17	3.29 ± 0.72
1.15–1.175	5.99 ± 0.18	2.71 ± 0.31
1.175–1.2	7.22 ± 0.18	3.25 ± 0.51
1.2–1.25	7.95 ± 0.13	4.72 ± 0.39
1.25–1.3	8.51 ± 0.13	4.20 ± 0.24
1.3–1.35	7.76 ± 0.12	5.88 ± 0.26
1.35–1.4	7.19 ± 0.13	6.90 ± 0.31
1.4–1.45	6.73 ± 0.12	6.65 ± 0.19
1.45–1.5	6.32 ± 0.12	7.37 ± 0.20
1.5–1.55	6.51 ± 0.13	7.56 ± 0.19
1.55–1.6	6.18 ± 0.13	7.60 ± 0.20
1.6–1.65	6.32 ± 0.13	6.82 ± 0.14
1.65–1.7	6.75 ± 0.14	5.93 ± 0.12
1.7–1.8	6.37 ± 0.10	5.73 ± 0.09
1.8–1.9	6.67 ± 0.11	5.99 ± 0.08
1.9–2.0	6.80 ± 0.11	5.83 ± 0.08
2.0–2.1	6.50 ± 0.11	5.55 ± 0.08
2.1–2.2	6.15 ± 0.11	5.76 ± 0.09
2.2–2.3	5.64 ± 0.11	5.57 ± 0.09
2.3–2.4	5.52 ± 0.11	5.70 ± 0.08
2.4–2.5	4.86 ± 0.11	5.75 ± 0.10
2.5–2.6	4.79 ± 0.13	6.27 ± 0.12

We gratefully acknowledge the help of the technical staff of the "Physikalisches Institut" and the engagement of the ELSA accelerator group. Our special thanks go to U. Mosel and G. Penner for providing us with the recent results of their calculation. This work is supported in part by the Deutsche Forschungsgemeinschft (DFG) (SPP KL 980/2-3).

References

1. J. Barth, *Photoproduktion von ω- und Φ-Mesonen bei Photonenergien bis 2.6 GeV*, PhD Thesis (German), BONN-IR-02-06, Bonn University, May 2002, ISSN-0172-8741.
2. J. Ballam *et al.*, Phys. Rev. D **7**, 3150 (1973).
3. R. Koniuk, Nucl. Phys. B **195**, 452 (1982); S. Capstick, CEBAF-TH-93-18; S. Capstick, W. Roberts, nucl-th/0008028; S. Capstick, Phys. Rev. D **46**, 2864 (1992); S. Capstick, W. Roberts, Phys. Rev. D **49**, 4570 (1994).
4. W.J. Schwille *et al.*, Nucl. Instrum. Methods Phys. Res. A **344**, 470 (1994).
5. Aachen-Berlin-Bonn-Hamburg-Heidelberg-München Collaboration, Phys. Rev. **175**, 1669 (1968).
6. Aachen-Hamburg-Heidelberg-München Collaboration, Nucl. Phys. B **108**, 45 (1976).
7. Particle Data Group (D.E. Groom *et al.*), Eur. Phys. J. C **15**, 1 (2000), (URL: `http://pdg.lbl.gov`).
8. K. Schilling, P. Seyboth, G. Wolf, Nucl. Phys. B **15**, 397 (1970).

9. W.E. Frahn, R.H. Venter, Ann. Phys. (N.Y.) **24**, (1963); B. Kozlowsky, A. Dar, Phys. Lett. **20**, 3 (1966).
10. F.J. Gilman, J. Pumplin, A. Schwimmer, L. Stodolsky, Phys. Lett. B **31**, 387 (1970).
11. ZEUS Collaboration, Z. Phys. C **73**, 73 (1996).
12. B. Friman, M. Soyeur, Nucl. Phys. A **600**, 477 (1996).
13. Y. Oh *et al.*, Phys. Rev. C **63**, 025201 (2001).
14. Q. Zhao *et al.*, Phys. Rev. C **58**, 2393 (1998).
15. Q. Zhao *et al.*, Phys. Lett. B **436**, 42 (1998).
16. Q. Zhao, Phys. Rev. C **63**, 025203 (2001).
17. G. Penner, PhD Thesis, Justus Liebig Universität Gießen, Fachbereich 07, 2002; G. Penner, U. Mosel, Phys. Rev. C **66**, 055211; 055212 (2002), e-Print Archive: nucl-th/0207069, nucl-th/0207066.
18. F.-J. Klein *et al.*, πN Newsl. **14**, 141 (1998).
19. H.R. Crouch *et al.*, Phys. Rev. **155**, 1476 (1967).
20. J.J. Manak, Nucl. Phys. A **663**, 671c (2000).